Downloaded from https://academic.oup.com/mnras/article/524/4/5446/7232535 by UCLA user on 08 September 2023

ROYAL ASTRONOMICAL SOCIETY

Strong lensed QSOs with variability detectable by LSST: How many are there?

Yoon Chan Taak [®]★ and Tommaso Treu [®]

Department of Physics and Astronomy, University of California, Los Angeles, CA 90095-1547, USA

Accepted 2023 July 19. Received 2023 July 19; in original form 2023 April 5

ABSTRACT

Strong lensed quasi-stellar objects (QSOs) are valuable probes of the Universe in numerous aspects. Two of these applications, reverberation mapping and measuring time delays for determining cosmological parameters, require the source QSOs to be variable with sufficient amplitude. In this paper, we forecast the number of strong lensed QSOs with sufficient variability to be detected by the Vera C. Rubin Telescope Legacy Survey of Space and Time (LSST). The damped random walk model is employed to model the variability amplitude of lensed QSOs taken from a mock catalogue by Oguri & Marshall (2010). We expect 30–40 per cent of the mock lensed QSO sample, which corresponds to ~1000, to exhibit variability detectable with LSST. A smaller subsample of 250 lensed QSOs will show larger variability of >0.15 mag for bright lensed images with i < 21 mag, allowing for monitoring with smaller telescopes. We discuss systematic uncertainties in the prediction by considering alternative prescriptions for variability and mock lens catalogue with respect to our fiducial model. Our study shows that a large-scale survey of lensed QSOs can be conducted for reverberation mapping and time delay measurements following up on LSST.

Key words: gravitational lensing: strong – quasars: general – quasars: supermassive black holes – cosmology: observations.

1 INTRODUCTION

Quasi-stellar objects (QSOs) are one of the brightest objects in the Universe, making them excellent probes to study the distant Universe (Kim et al. 2015, 2019, 2020, 2022; Bañados et al. 2016; Jeon et al. 2016, 2017; Jiang et al. 2016; Wang et al. 2021). Their extreme luminosities, sometimes outshining their host galaxies, are powered by gas accretion into the central supermassive black hole (SMBH).

The mass of the supermassive black hole $(M_{\rm BH})$ at the QSO centre is a crucial property used for understanding not only the history of SMBHs, but also their seeming coevolution with their host galaxies (Ferrarese & Merritt 2000; Gebhardt et al. 2000; Kormendy & Ho 2013). Among the three main methods for measuring $M_{\rm BH}$, the most reliable method uses the dynamics of gas clouds and stars rotating around the SMBH based on simple Newtonian dynamics (e.g. Ghez et al. 2008; Cappellari et al. 2009), but this is only feasible for local SMBHs for which the orbit can be precisely monitored.

Reverberation mapping (RM), in which the sphere of influence of the black hole is resolved in time rather than in angles, is commonly used for more distant SMBHs (Blandford & McKee 1982; Fromerth & Melia 2000; Peterson et al. 2004; Shen et al. 2015b). The broad-line region (BLR) is excited by the continuum emitted from the accretion disc, so fluctuations in the continuum are mirrored in the emission line light curve with a time lag, which is interpreted as the light traveltime to the BLR. This lag is traditionally used as the distance in a virial estimator, while the line widths of the variable portion of the broad lines represent the velocity component, and the virial coefficient is estimated empirically. Alternatively, forward modelling of velocity-resolved RM can provide a self-

The downsides of RM are twofold; the first is the large number of epochs required for monitoring, and the second is the signal-tonoise ratio (SNR) of the observations required to detect variability. It is much easier to obtain high-SNR spectra for bright OSOs, but in general these are less variable and therefore detecting variability requires high SNR (Suberlak, Ivezić & MacLeod 2021, hereafter S21), so long exposure times per epoch are necessary regardless of the intrinsic luminosity. In addition, the expected time lags for bright QSOs are in the range of 10^{2-4} d, which needs to be multiplied by a factor of $(1 + z_s)$ to account for time dilation. The cost of an RM campaign is further exacerbated by the fact that the monitoring baseline needs to be at least several times longer than the observed time lag to detect the fluctuations (Shen et al. 2015a), implying that the required monitoring periods for bright and distant QSOs are of decade-scales (Kaspi et al. 2017).

Both shortcomings of the technique can be mitigated by observing gravitationally lensed QSOs. Gravitational lensing occurs when a light source is located directly behind a massive object. When

consistent mass estimate with higher precision, without relying on external calibrations of the virial coefficient (e.g. Pancoast, Brewer & Treu 2014; Williams et al. 2018; Villafaña et al. 2022; Williams & Treu 2022). An important byproduct of RM is the so-called singleepoch method, which also uses the virial theorem to estimate $M_{\rm BH}$ (Vestergaard & Peterson 2006; Vestergaard & Osmer 2009); here, the BLR size (R_{BLR}) is approximated from the monochromatic luminosity via the empirical BLR size-luminosity (R_{BLR} -L) relation (Kaspi et al. 2000, 2005; Bentz et al. 2013). Unfortunately there are many factors of uncertainty in this methodology, such as which line width measurements best represent what is used in RM (Assef et al. 2011; Denney et al. 2013, 2016), the intrinsic scatter of the $R_{\rm BLR}$ –L relation, and the unknown virial coefficient. Thus, RM is arguably the best way to measure $M_{\rm BH}$, in terms of both accuracy and versatility.

the background source is a point source, like a QSO, this results in multiple images, whose luminosities are usually magnified; the magnification enables us to measure both the continuum and emission line fluxes at lower observational cost, sometimes even for OSOs that have intrinsic brightnesses below the detection limit of a given telescope and instrument combination. A second characteristic of lensed QSOs is time delays; the multiple images of the same source QSO travel through different light paths depending on the configuration of the source and deflector, so a time delay arises between any image pair. If the multiple images are monitored simultaneously, one effectively obtains multiple epochs at once, thus reducing the requirements in terms of sampling and duration of an RM campaign. A recent study has successfully conducted RM for a distant gravitationally lensed QSO, effectively extending the intrinsic light curves by two years with respect to the duration of the monitoring period (Williams et al. 2021). Both effects are most relevant for distant sources, where only bright QSOs can be seen (and thus magnification will be important) and the time dilation effect is the greatest.

Another application of lensed QSOs is that they can be used to constrain cosmological parameters. The time delays among the multiple images depend not only on the deflector-source configuration but also on the parameters of the Universe. This allows one to measure the Hubble constant (H_0) with high precision that is completely independent of other methodologies (see e.g. Treu, Suyu & Marshall 2022 for a recent review). This technique has the potential to help solve the so-called 'Hubble tension', i.e. the tension between low and high redshift measurements of the Hubble constant H_0 (Abdalla et al. 2022).

A key aspect in both the applications of lensed QSOs mentioned above is that the source QSOs need to be variable. Although the variable nature of QSOs has been recognized since their discovery and studied for decades (Matthews & Sandage 1963; Smith & Hoffleit 1963), the exact mechanism behind it is still not fully understood (Hawkins 2002). Fortunately, the mechanism of the QSO variability is unimportant in both cases, and only the phenomenon of variability itself is critical for monitoring purposes. Thus, an empirical description of the variability is sufficient for these applications.

The magnitude and time-scale of the variability are thought to depend on specific parameters of the QSO, such as its luminosity (Giveon et al. 1999). Unfortunately the correlations are difficult to confirm, to the extent that even the direction of the correlations are ambiguous from study to study (see discussions in Giveon et al. 1999 and S21); biased samples and imperfect light curves used in the analyses have been cited as some of the causes. The most successful practical model so far has been the damped random walk (DRW) model (Kelly, Bechtold & Siemiginowska 2009). MacLeod et al. (2010, 2012) have demonstrated that this model can be applied to large samples of individual QSO light curves as well, and S21 present updates with longer observation baselines. Even though modifications to this simple approach could provide an even better description of individual QSO light curves (Kelly et al. 2014), DRW suffices for most applications.

In this paper, we estimate how many lensed QSOs in the Legacy Survey of Space and Time (LSST) will exhibit sufficiently large variability and luminosity to be suitable candidates for RM or measuring time delays. Section 2 illustrates the methodology. Results are shown in Section 3, and discussed in Section 4. The paper is concluded in Section 5. Throughout this paper, we use the AB magnitude system (Oke & Gunn 1983) and a standard Lambda cold dark matter cosmology with $H_0=70\,\mathrm{km\,s^{-1}}$ Mpc⁻¹, $\Omega_\mathrm{M}=0.3$ and $\Omega_\Lambda=0.7$, unless specified otherwise.

2 METHODOLOGY

We start with the lensed QSO mock catalogue provided by Oguri & Marshall (2010, hereafter OM10). The catalogue contains 15 658 mock lensed QSOs over a 100 000 deg² area, and the parameters of the deflectors and sources for each lensed QSO, such as redshifts of the deflector and source, magnitudes of the source and lensed images, and time delays. For our predictions, we use some parameters that already exist in the catalogue, and compute some additional parameters discussed below. Finally, to match with the expected LSST areal coverage of 20 000 deg², we scale the numbers by 1/5 for a sample of 3131.6 lensed QSOs. We note that the cosmology used for the catalogue assumes $\Omega_{\rm M}=0.26$, which is different from what is used in other parts of our paper, but we do not expect this difference to be significant for our purposes.

2.1 Asymptotic structure function

To model the variability, we follow the DRW model for Sloan Digital Sky Survey (SDSS) QSOs shown in S21. From a time-series light curve of a QSO, we can calculate the structure function (SF), which is the root-mean-squared scatter of magnitude differences for a fixed time difference Δt . This is related to the autocorrelation function as

$$SF^{2}(\Delta t) = 2S^{2}[1 - ACF(\Delta t)], \tag{1}$$

where S^2 is the variance and ACF is the autocorrelation function (Emmanoulopoulos, McHardy & Uttley 2010; note that SF is defined differently here). For DRW processes, this can be expressed as an exponentially converging function in the form of

$$SF(\Delta t) = SF_{\infty} [1 - \exp(-\Delta t/\tau)]^{1/2}, \tag{2}$$

where SF_{∞} is the asymptotic SF for large Δt and τ is a characteristic time-scale. We treat SF_{∞} as the magnitude of the variability, in that if SF_{∞} is larger than the magnitude errors (S21, fig. 8) we regard the QSO variability to be detectable. We obtain the predicted magnitude errors for LSST from equation (5) of Ivezić et al. (2019), reproduced here as

$$\sigma_{\text{rand}}^2 = (0.04 - \gamma)x + \gamma x^2,$$
(3)

where $\sigma_{\rm rand}$ is the random photometric error for point sources, $\gamma = 0.039$ is a factor depending on elements such as sky brightness and readout noise, and $x \equiv 10^{0.4(m-m_5)}$, with $m_5 = 23.92$ mag being the 5σ depth. γ and m_5 values are taken from table 2 of Ivezić et al. (2019) for the *i*-band filter.

Thus, SF_{∞} and τ are necessary to estimate the SF for a given QSO to check its variability levels. Fortunately, by fitting a large sample of QSOs (S21), both SF_{∞} and τ can be modelled as functions of observable parameters of the QSO, namely its absolute magnitude and SMBH mass as

$$\log f = A + B \log \frac{\lambda_{\text{RF}}}{4000 \,\text{Å}} + C(M_i + 23) + D \log \frac{M_{\text{BH}}}{10^9 \,\text{M}_{\odot}}, \quad (4)$$

where f is either SF_{∞} or τ , λ_{RF} is the rest-frame wavelength, M_i is the i-band absolute magnitude, M_{BH} is the mass of the SMBH, and A through D are the coefficients shown in table 2 of S21. An additional parameter, the QSO redshift, was found to have a negligible effect on the variability parameters (MacLeod et al. 2010). Among the three coefficient sets in the table, we use those for the SDSS-Pan-STARRS1 (PS1) combined light curves.

Since $M_{\rm BH}$ is not a given quantity in the OM10 catalogue, we estimate it from the QSO luminosity following Taak & Im (2020), and describe this procedure here concisely. QSO absolute magnitudes are

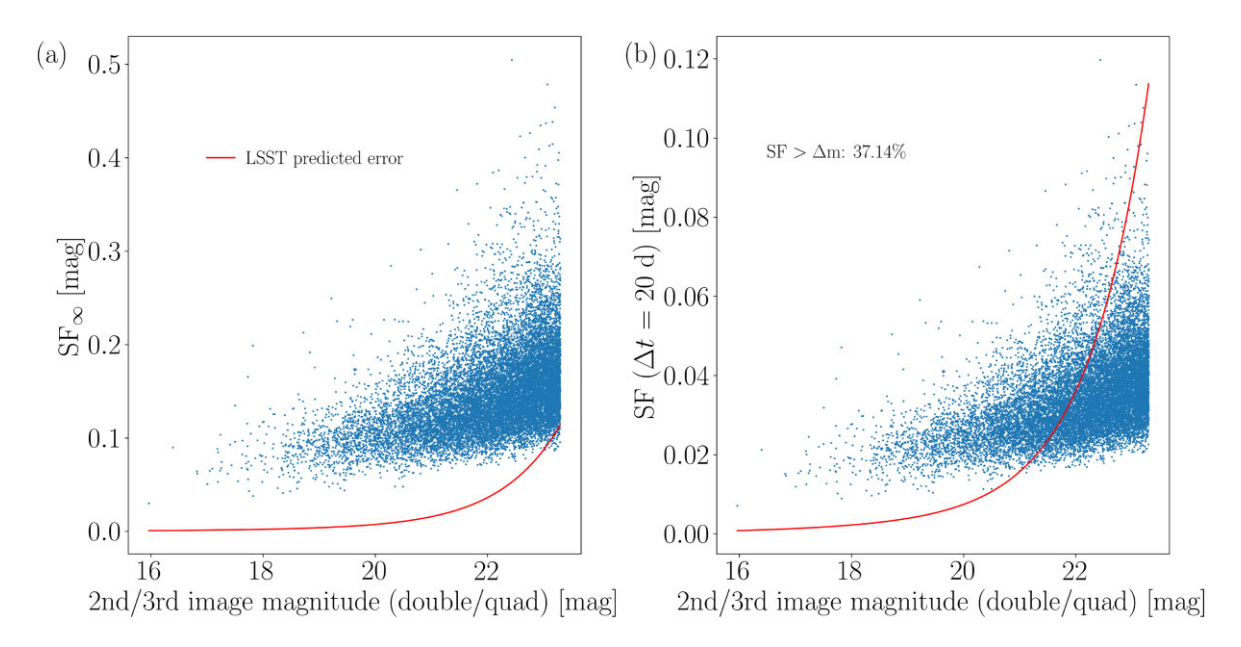


Figure 1. (a) Scatter plot of SF_{∞} versus the reference magnitude for the lensed QSO sample from OM10. The red solid line denotes the predicted error for single-epoch LSST observations (Ivezić et al. 2019) as a reference for the approximate level of variability that will be detectable. (b) Scatter plot of the structure function for $\Delta t = 20 \,\mathrm{d}$ versus the reference magnitude.

traditionally given in the i filter at z=2 ($M_{i,z=2}$), which corresponds to rest-frame wavelengths of roughly 2200–2800 Å (Richards et al. 2006), to minimize the K-corrections for the various QSO redshifts. For QSOs within a specific $M_{i,z=2}$ bin, the $M_{\rm BH}$ distribution can be fit as a Gaussian function. The mean $M_{\rm BH}$ of this Gaussian for all $M_{i,z=2}$ bins is a linear function of $M_{i,z=2}$ [fig. 4(b) of Taak & Im 2020], so we can estimate the $M_{\rm BH}$ of a QSO as $\log{(M_{\rm BH}/M_{\odot})}=2.5-0.25\,M_{i,z=2}$ with errors of \sim 0.3 dex. This estimate is in agreement with fig. 21(a) of S21, thus demonstrating the validity of the method. Since the values for coefficients C and D are comparable, this equation suggests that the overall dependence of SF $_{\infty}$ on the QSO brightness is negative, i.e. brighter QSOs are less variable, as expected.

For two-image lens systems (doubles), the variability of the dimmer image determines whether a lensed QSO can be used for either RM or H_0 measurements; for four-image lens systems (quads), detection and monitoring of at least the third-brightest image is necessary to make use of information content beyond that of a double (OM10). Thus, we introduce the 'reference' magnitude, which is the magnitude of either the dimmer image for doubles or that of the third-brightest image for quads.

2.2 BLR size

For RM purposes, $R_{\rm BLR}$ allows us to estimate the observation duration required for measuring the time lags. It can be predicted from the luminosity of the AGN using the empirical relation (Bentz et al. 2013)

$$\log \frac{R_{\rm BLR}}{\text{lt-days}} = 1.527 + 0.533 \log \frac{L_{5100}}{10^{44} \text{ erg s}^{-1}},\tag{5}$$

where L_{5100} is the monochromatic luminosity of the AGN at 5100 Å. We estimate the observed time lag by using this BLR size multiplied by a factor of (1 + z) to account for time dilation.

3 RESULTS

Fig. 1(a) shows the scatter plot of SF_{∞} versus the reference magnitude. As expected from equation (4), lensed QSOs with fainter images have a tendency to be marginally more variable with larger scatter. Fig. 1(b) shows a similar plot with $SF(\Delta t)$ with $\Delta t = 20$ d instead, to visualize the actual magnitude differences for a LSST-like cadence. The shape of the scatter plots are similar apart from a scaling factor, indicating that $SF(\Delta t = 20$ d) is simply SF_{∞} reduced by a factor of \sim 5. We assume for simplicity that the QSO variability can be detected if $SF(\Delta t)$ is larger than the predicted magnitude errors (Δm) for LSST (Ivezić et al. 2019, equation 5), which are also plotted for comparison. Using this argument, we estimate that variability will be detectable for 37 per cent of the lensed QSO population.

Fig. 3 shows the scatter plots of various properties of the lensed QSOs computed in the previous section. In the previous section we discussed the detectability of variability. In this section we focus on quantifying the size of subsamples that would be ideal for RM and time delays studies, i.e. those that exhibit bright lensed images with large variability. 'Bright' and 'large' in this context depend mostly on the observational resources that one has available, and there is certainly a degree of subjectivity in presenting any specific choice. We present some for illustration, making the full code available to the reader, in case they want to pursue their own selection.¹

The cuts applied for the first subsample (Subsample 1) are $SF_{\infty} > 0.15$ and $i_1 < 21$ mag, where i_1 is the magnitude of the brightest image; these numbers represent variability scales that can be readily monitored by two- to four-metre-class telescopes (Shen et al. 2015a). The number of lensed QSOs satisfying these conditions is 243.4 for a 20 000 deg² areal coverage. We apply a second set of cuts that chooses a smaller subsample, Subsample 2, displaying larger variability for brighter images. The cuts applied for Subsample 2 are $SF_{\infty} > 0.20$ and $i_1 < 20$ mag, and the number of lensed QSOs in this subsample

¹The code will be available at https://github.com/yctaak/Lensed-QSO-Varia bility upon acceptance of the paper.

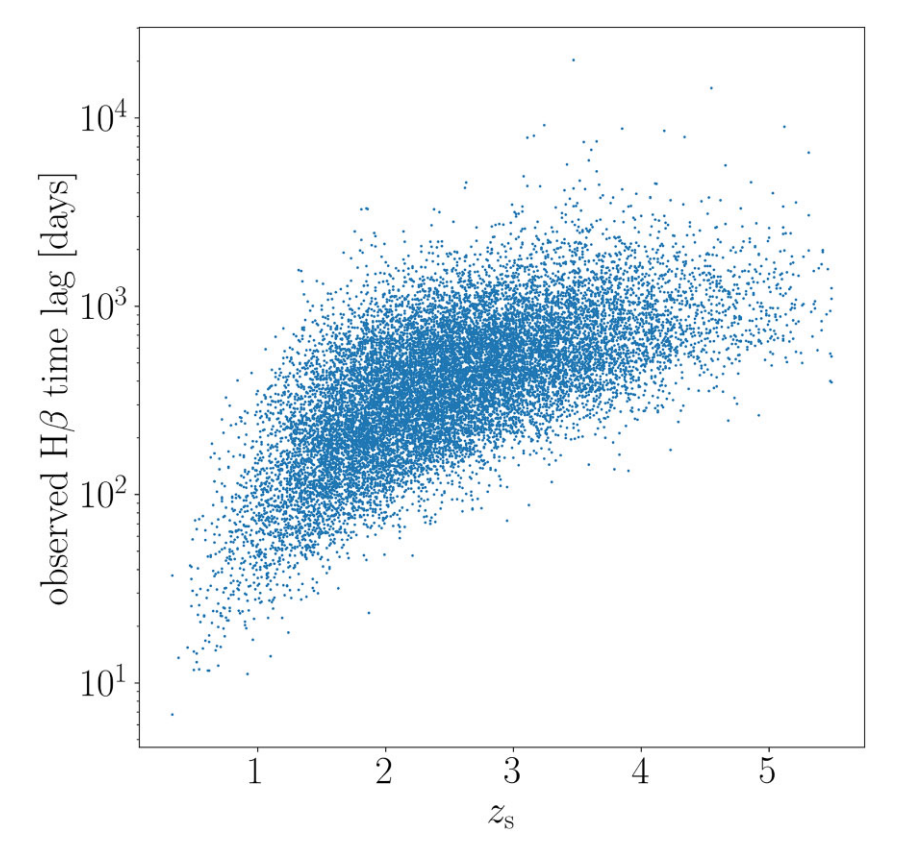


Figure 2. Scatter plot of the expected observed time lag for the H β line versus the source redshift for the lensed QSO sample from OM10.

is 7.0. These numbers demonstrate that there is a significant number of lensed QSOs within the LSST areal coverage, to be followed up with two- to four-metre-class telescopes. Clearly, a follow-up with larger telescopes would have access to a much larger subsample. For example, Williams et al. (2021) monitored a source of apparent magnitude $i \sim 20$ –21 using the Gemini North 8-m Telescope, achieving velocity-resolved RM measurements. Likewise, high-cadence monitoring with milli-magnitude precision would be able to determine gravitational time delays even with small variability amplitude over a relatively short time-scale (Courbin et al. 2018).

The distributions of some of the lensed QSO properties for the full sample and each subsample are shown in Fig. 4. The distributions for the deflector properties are similar between the three samples (Subsamples 1, 2, and the full sample) except for an overall scale-factor difference, suggesting that there are no selection effects due to the subsamples regarding the deflector population. We note that the number of lensed QSOs with $z_{\rm s} > 1$ account for at least one half of each subsample, demonstrating a plethora of distant targets for RM, which benefit the most from the use of lensed QSOs due to the effect of time dilation as was discussed in the introduction.

An important statistic of the lensed QSOs is the quad fraction (Lemon et al. 2020). Quads tend to have larger magnifications when compared to doubles, making them more effective in terms of shortening individual monitoring epochs. They are also more practical for time delay cosmography because it is possible to measure six time delays between each image pair allowing better lens modelling, in contrast to the single time delay for doubles. Unfortunately this is not true for RM since the time delay acts by effectively extending the monitoring time span, so the length of the maximum time delay between the images is the crucial factor.

We calculate the quad fraction for each of our (sub)samples and display them in Fig. 3. The full sample of lensed QSOs has a quad fraction of about one-seventh, and this is increased subsequently by factors of roughly two and four for Subsamples 1 and 2, respectively. This increase may be caused by either the higher variability cut or the higher luminosity cut; quads magnify the sources more, so the luminosity increase is trivial, but this also means that the quads are intrinsically fainter, meaning that they are more variable.

To check which factor has a stronger effect, we conduct a simple exercise by creating two additional subsamples that use intervening cuts; one with $SF_{\infty} > 0.15$ and $i_1 < 21$, and another with $SF_{\infty} > 0.20$ and $i_1 < 20$. We expect these new subsamples to have quad fractions somewhere between those for Subsamples 1 and 2, and they do indeed with 0.417 and 0.394, respectively. Unfortunately the two values are too close to each other to conclude which is the more dominant factor, and we conclude that both the variability and the luminosity cuts influence the quad fraction with similar strengths.

It is possible to determine whether area or depth is more important for these lensed QSOs. Following Taak & Im (2020), we consider two surveys with identical observation times, with one survey aiming for depth and the other for wider area. If the area ratio is 1:10, the deeper survey should have a limiting magnitude that is 1.25 mag deeper. So for the deeper survey to yield as many lensed QSOs as the wider survey, the slope of the magnitude histogram must be (log 10)/1.25 = 0.8. Fig. 5 shows the histogram of the reference magnitude for the full sample and two subsamples. We can see that the slope of 0.8 is only achievable for shallow surveys, implying that for depths similar to those for LSST, a wider area should be prioritized over depth to maximize the lensed QSO sample size, which is what has been done for LSST.

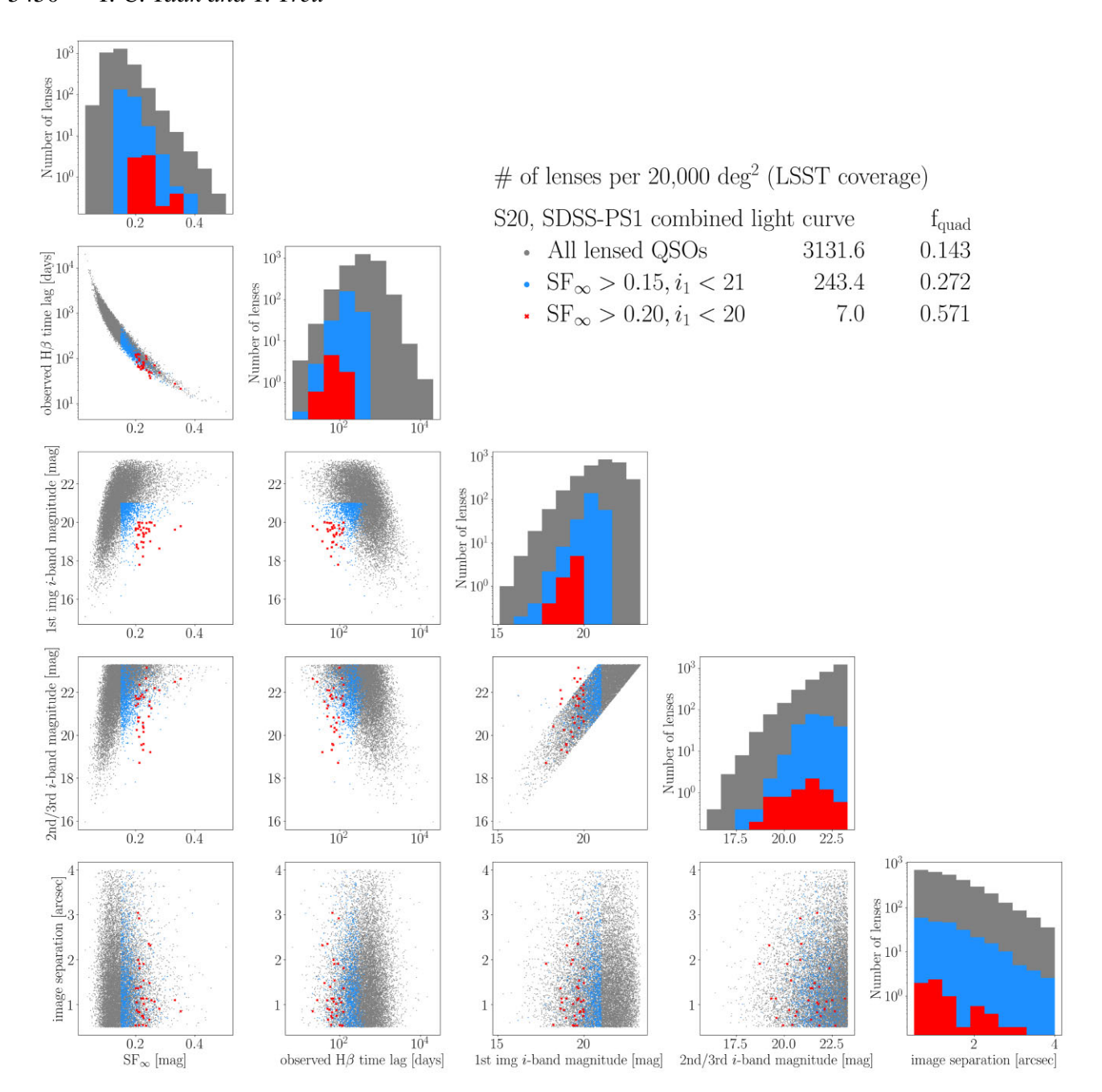


Figure 3. Scatter plots of several parameters of the OM10 lensed QSO sample. Grey dots indicate the full sample, while blue dots and red crosses represent the subsamples of lensed QSOs with SF_{∞} and i_1 cuts. The number of lensed QSOs in each sample scaled for a fiducial LSST-like areal coverage are shown on the figure, along with the quad fraction for each subsample. The scatter plots show the samples for the unscaled $100\,000\,\text{deg}^2$ areal coverage, while the histograms for each parameter on the diagonal show the scaled numbers.

The expected time lags for H β are plotted versus the source redshift in Fig. 2. The lags range between tens to thousands of days, demonstrating the appeal of using lensed QSO time delays to decrease the monitoring period.

4 DISCUSSION: SOURCES OF UNCERTAINTY

4.1 Variants to SF_{∞} computation

Table 2 of S21 provides three distinct sets of coefficients for SF_{∞} and τ , depending on the light curves used for the analysis and the

method used for obtaining the coefficients. The first and second sets use SDSS-only light curves which span $\sim \! 10 \, \mathrm{yr}$ and are used in MacLeod et al. (2010), while the final coefficient set uses SDSS-PS1 combined light curves, which effectively extends the timeline to 15 yr. The difference between the first and second coefficient sets is that the first set provides the best-fitting coefficients (labeled as the M10 method) while the second set uses likelihood distributions to calculate the expectation values (labeled as the S20 method, in line with the notation in S21). The final coefficient set, which is the one used in Section 2.1, also uses the S20 method, but is derived from the best fits to the SDSS-PS1 combined light curves,

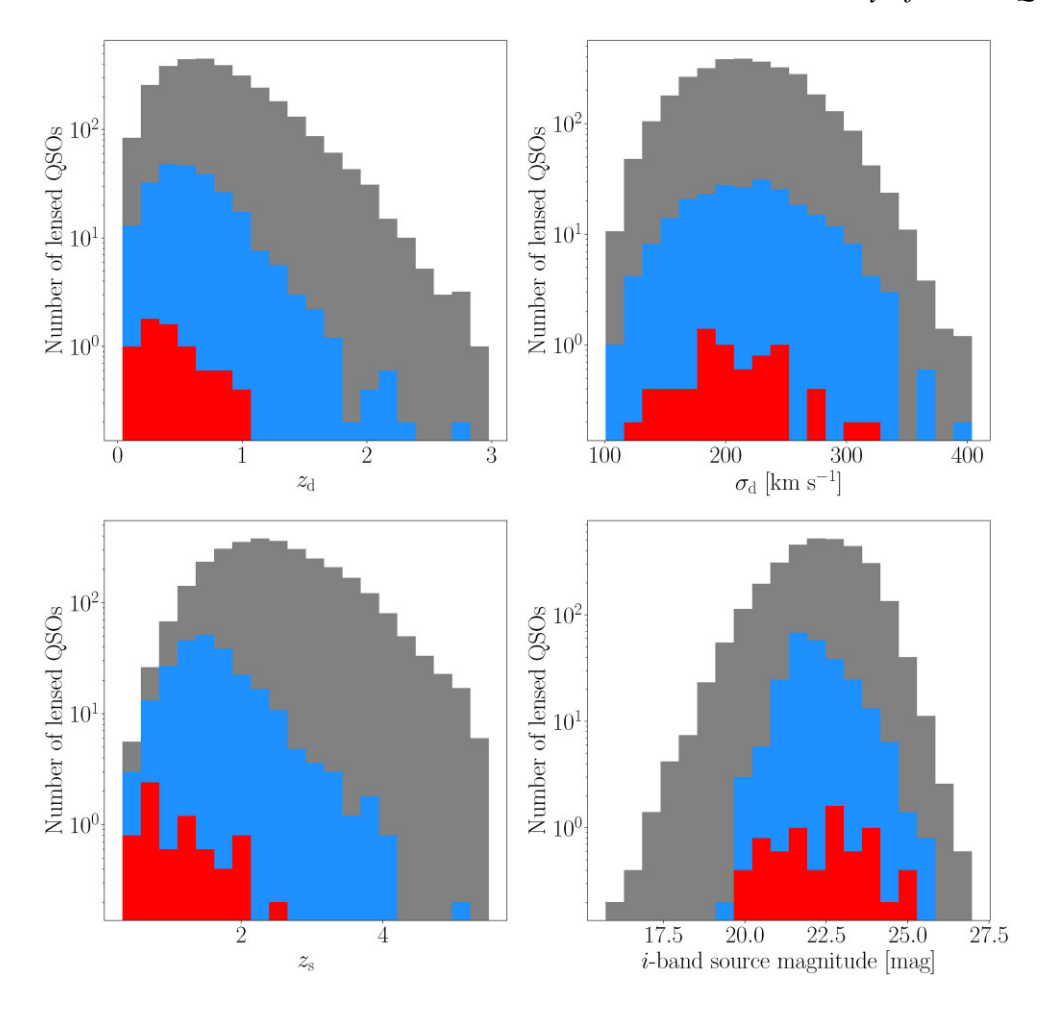


Figure 4. Histogram of the deflector and source properties for the OM10 sample. Numbers are scaled for a 20 000 deg² areal coverage. Top row: deflector redshift and deflector velocity dispersion. Bottom row: source redshift and *i*-band source magnitude. Colours are identical to those in Fig. 3.

which we trust to be more reliable due to its longer observation baseline.

To test the robustness of our results with respect to the various approaches used to estimate the variability, we recalculate the number of lensed OSOs that satisfy our selection cuts using the other two coefficient sets for the SDSS light curves shown in table 2 of S21. The number of lensed QSOs satisfying the two conditions for SF_{∞} and i_1 (Subsamples 1 and 2) are summarized in Table 1. Based on these numbers, we conclude that the number of bright and variable lensed OSOs may be decreased by a factor of 2 with respect to the numbers shown in Section 3, depending on the coefficient set used for the SF_{∞} computation. We can see that the sample sizes for both subsamples decrease in the following order: S20/SDSS-PS1, M10/SDSS, S20/SDSS. The main reason for this difference is the change in the offset of the coefficient sets, A, for SF_{∞} ; the values of A decrease in the same order, meaning that SF_{∞} becomes smaller in the same order, and consequently the number of lensed QSOs satisfying the subsample cut decreases. The fraction of all lensed QSOs that have SF(Δt) larger than its predicted magnitude error for LSST-like observations changes from 37 per cent for the coefficient set using the SDSS-PS1 combined light curve to 41 per cent and 34 per cent for the two coefficient sets using the SDSS-only light curve.

We also consider the effect of Δt on $SF(\Delta t)$. In Fig. 1(b), $SF(\Delta t)$ was calculated based on a 20-d cadence, which is obtained by dividing the 10-yr survey period by the mean number of visits of the

full survey area, which is about 180 for the *i*-band filter. This does not reflect the actual time duration between images; with the current observing strategy, each pair of visits is planned to be conducted within an hour separation, and the visibility of the sky position usually requires seasonal changes. Accounting for just these two factors will yield a cadence similar to 20 d; but we inspect how the fraction of lensed QSOs with detectable variability for some other cadences. We expect shorter cadences to decrease $SF(\Delta t)$ based on equation (2), which implies that the fraction of lensed QSOs with variability larger than the magnitude errors should decrease also. For cadences between 10 and 40 d, the variability-detectable fraction varies from 25 per cent to 53 per cent, which indicates a \sim 0.15 dex range from the original fraction of 37 per cent.

4.2 Updated lensed QSO mock catalogue

The OM10 catalogue uses a deflector velocity dispersion function (VDF) that is constant over cosmic time, along with an outdated version of the redshift-dependent QSO luminosity function (LF). Yue et al. (2022) have updated this catalogue in three major aspects; first by employing a revised VDF from the CosmoDC2 mock galaxy catalogue (Korytov et al. 2019) which allows for a redshift evolution of the deflector VDF, second by using a QSO LF which includes the latest discoveries especially at higher redshifts, and third by extending the image separation limit down to \sim 0.1 arcsec. We select

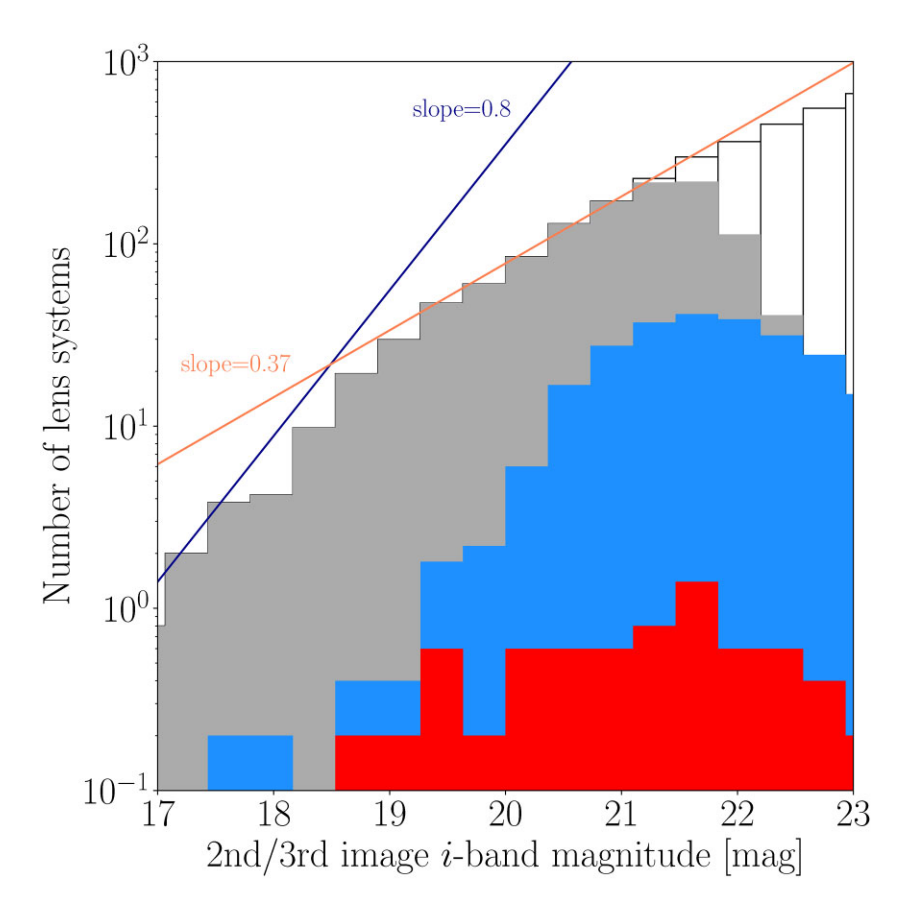


Figure 5. Histogram of the reference magnitude for the three subsamples. The empty and grey histograms represent the full sample and the $SF(\Delta t = 20 \text{ d}) > \Delta m$ subsample, respectively, and the blue and red histograms correspond to Subsamples 1 and 2, respectively. The dark blue line indicates a slope of 0.8 corresponding to depth—width equivalence, while the pink line corresponds to the slope of the histogram at $i_{ref} \sim 20$ mag.

Table 1. Number of lensed QSOs for a LSST-like areal coverage with bright images and large variability.

Method ^a and light curve	$SF_{\infty}>0.15, i_1 < 21 \text{ mag}$ (Subsample 1)	$SF_{\infty}>0.2, i_1 < 20 \text{ mag}$ (Subsample 2)	Fraction of lensed QSOs with $SF(\Delta t = 20 \text{ d}) > \Delta m$
S20/SDSS-PS1	243.4	7.0	0.371
M10/SDSS	211.0	6.2	0.407
S20/SDSS	105.2	3.8	0.343

a S20 denotes the method used in S21, in line with the notation within the paper. M10 denotes the method used in MacLeod et al. (2010).

lensed QSOs with reference magnitudes brighter than the LSST single-visit depth of i=23.3 mag and image separations larger than 0.5 arcsec for direct comparison with the OM10 catalogue. For the SF $_{\infty}$ calculation, we use only the S20 method for the SDSS-PS1 combined light curve for comparison purposes. The number of lensed QSOs are scaled to match the fiducial areal coverage of 20 000 deg².

The results are as follows; the number of lensed QSOs for a LSST-like areal coverage is 813.0, and the sizes of Subsamples 1 and 2 are 42.5 and 1.0, respectively. The (sub)sample sizes are smaller than those for the OM10 catalogue by a factor of \sim 4–7, which can be explained by the differences in the VDF and QSO LF used for the two catalogues.

4.3 Range of θ_{Ein}

The OM10 catalogue contains galaxy-scale deflectors only, with limits to the image separation at 0.5 arcsec and 4 arcsec. Lensed QSOs with larger image separations for group or cluster-scale deflectors

will be especially useful for RM studies due to their longer and thus easier-to-measure time delays. As discussed earlier, these longer time delays will be most effective for the reduction of the monitoring baseline. Therefore we should consider our estimate conservative in this regard, since systems with wider image separation should be discoverable within LSST, as they have been discovered in SDSS.

At the other end of the spectrum, the distribution of the Einstein radii of galaxy-scale deflectors (Collett 2015; Taak & Im 2020) suggests that there is a plethora of lensed QSOs with smaller image separations. Unfortunately these small-separation lensed QSOs will be difficult to monitor with ground-based telescopes such as LSST due to atmospheric seeing. Thus, our estimates are conservative in this respect as well.

5 CONCLUSION

In this paper, we demonstrate the methodology for computing the number of lensed QSOs that are sufficiently bright and variable for

Jeon Y., Im M., Pak S., Hyun M., Kim S., Kim Y., Lee H.-I., Park W., 2016,

Hawkins M. R. S., 2002, MNRAS, 329, 76

Ivezić Ž. et al., 2019, ApJ, 873, 111

RM and H_0 measurements with LSST. Among the 3131.6 lensed QSOs in the OM10 mock catalogue, 30–40 per cent will show variability larger than the LSST magnitude errors, and 100–250 of them are bright and significantly variable. An updated version of the mock catalogue suggests a factor of \sim 5 decrease in these numbers. These numbers indicate that plenty of lensed QSOs exhibit sufficient variability for monitoring with small telescopes, and many more will be monitored systematically with LSST. The calculations performed in this paper, and the software that is publicly released with it, will help designing future studies for either RM or time delay measurements.

ACKNOWLEDGEMENTS

We thank Masamune Oguri, Philip J. Marshall, Minghao Yue, and Matt Malkan for providing valuable discussions. This research was supported by the Basic Science Research Program through the National Research Foundation of Korea (NRF) funded by the Ministry of Education (grant number 2021R1A6A3A14044070).

DATA AVAILABILITY

The code for the subsample selection process, along with its resulting catalogue, will be available at https://github.com/yctaak/Lensed-Q SO-Variability upon acceptance of the paper.

```
REFERENCES
Abdalla E. et al., 2022, J. High Energy Astrophys., 34, 49
Assef R. J. et al., 2011, ApJ, 742, 93
Bañados E. et al., 2016, ApJS, 227, 11
Bentz M. C. et al., 2013, ApJ, 767, 149
Blandford R. D., McKee C. F., 1982, ApJ, 255, 419
Cappellari M., Neumayer N., Reunanen J., van der Werf P. P., de Zeeuw P.
   T., Rix H. W., 2009, MNRAS, 394, 660
Collett T. E., 2015, ApJ, 811, 20
Courbin F. et al., 2018, A&A, 609, A71
Denney K. D., Pogge R. W., Assef R. J., Kochanek C. S., Peterson B. M.,
   Vestergaard M., 2013, ApJ, 775, 60
Denney K. D. et al., 2016, ApJS, 224, 14
Emmanoulopoulos D., McHardy I. M., Uttley P., 2010, MNRAS, 404, 931
Ferrarese L., Merritt D., 2000, ApJ, 539, L9
Fromerth M. J., Melia F., 2000, ApJ, 533, 172
Gebhardt K. et al., 2000, ApJ, 539, L13
Ghez A. M. et al., 2008, ApJ, 689, 1044
Giveon U., Maoz D., Kaspi S., Netzer H., Smith P. S., 1999, MNRAS, 306,
```

```
J. Korean Astron. Soc., 49, 25
Jeon Y. et al., 2017, ApJS, 231, 16
Jiang L. et al., 2016, ApJ, 833, 222
Kaspi S., Smith P. S., Netzer H., Maoz D., Jannuzi B. T., Giveon U., 2000,
   ApJ, 533, 631
Kaspi S., Maoz D., Netzer H., Peterson B. M., Vestergaard M., Jannuzi B. T.,
   2005, ApJ, 629, 61
Kaspi S., Brandt W. N., Maoz D., Netzer H., Schneider D. P., Shemmer O.,
   2017, Frontiers Astron. Space Sci., 4, 31
Kelly B. C., Bechtold J., Siemiginowska A., 2009, ApJ, 698, 895
Kelly B. C., Becker A. C., Sobolewska M., Siemiginowska A., Uttley P.,
   2014, ApJ, 788, 33
Kim Y. et al., 2015, ApJ, 813, L35
Kim Y. et al., 2019, ApJ, 870, 86
Kim Y. et al., 2020, ApJ, 904, 111
Kim Y. et al., 2022, AJ, 164, 114
Kormendy J., Ho L. C., 2013, ARA&A, 51, 511
Korytov D. et al., 2019, ApJS, 245, 26
Lemon C, et al., 2020, MNRAS, 494, 3491
MacLeod C. L. et al., 2010, ApJ, 721, 1014
MacLeod C. L. et al., 2012, ApJ, 753, 106
Matthews T. A., Sandage A. R., 1963, ApJ, 138, 30
Oguri M., Marshall P. J., 2010, MNRAS, 405, 2579 (OM10)
Oke J. B., Gunn J. E., 1983, ApJ, 266, 713
Pancoast A., Brewer B. J., Treu T., 2014, MNRAS, 445, 3055
Peterson B. M. et al., 2004, ApJ, 613, 682
Richards G. T. et al., 2006, AJ, 131, 2766
Shen Y. et al., 2015a, ApJS, 216, 4
Shen Y. et al., 2015b, ApJ, 805, 96
Smith H. J., Hoffleit D., 1963, Nature, 198, 650
Suberlak K. L., Ivezić Ž., MacLeod C., 2021, ApJ, 907, 96 (S21)
Taak Y. C., Im M., 2020, ApJ, 897, 163
Treu T., Suyu S. H., Marshall P. J., 2022, A&AR, 30, 8
Vestergaard M., Osmer P. S., 2009, ApJ, 699, 800
Vestergaard M., Peterson B. M., 2006, ApJ, 641, 689
Villafaña L. et al., 2022, ApJ, 930, 52
Wang F. et al., 2021, ApJ, 907, L1
Williams P. R., Treu T., 2022, ApJ, 935, 128
Williams P. R. et al., 2018, ApJ, 866, 75
Williams P. R. et al., 2021, ApJ, 911, 64
Yue M., Fan X., Yang J., Wang F., 2022, AJ, 163, 139
```

This paper has been typeset from a TEX/LATEX file prepared by the author.